CFD-DEM simulations of hydrodynamics of combined ion exchange-membrane filtration

Naukkarinen Tomi, Nikku Markku, Turunen-Saaresti Teemu

CFD-DEM simulations of hydrodynamics of combined ion exchange-membrane filtration

Tomi Naukkarinen[a,*], Markku Nikku[a], Teemu Turunen-Saaresti[a]

[a]*School of Energy Systems, Lappeenranta University of Technology, Lappeenranta, Finland*

Abstract

The combined ion exchange-membrane filtration system, whereby an active filtration layer is formed using a slurry flow of resin beads and water, has the potential to reduce energy usage and increase the quality of purified wastewater. The hydrodynamic design of these systems is in its infancy and there is a need for numerical methods to analyze such systems. In this work, computational fluid dynamics coupled with the discrete element method (CFD-DEM) is utilized to analyse the hydrodynamics of the combined ion exchange-membrane filtration system, and the formation of the filtrating bed and the parameters affecting it are studied by varying the flow conditions. As a result, the details of the bed formation with insights on the parameters affecting these phenomena and suggestions for an improved hydrodynamic design of the combined ion exchange-membrane filtration system are presented.

Keywords: CFD-DEM, combined-filtration, wastewater, resin beads

1. Introduction

Pharmaceuticals and personal care products (PPCPs) (e.g. hormonal contraception) as well as endocrine disturbing compounds (EDCs) (e.g. bisphenol A [BPA]) are passed in drinking water and food due to the reusing of wastewater as a source of drinking water ([1], [2]). According to the literature ([3], [4], [5] and [6]), these contaminants are common in municipal wastewater as a result

---

*Corresponding author
  Email address: Tomi.Naukkarinen@lut.fi (Tomi Naukkarinen)

of the extensive use of BPA and hormonal contraception. Population growth and the climate change are reducing available water resources per inhabitant, which increases the attractiveness of reusing the wastewater. Diminishing water resources have received attention from some public organizations, for example, the EU has a policy to promote wastewater reclamation and reuse to improve the state of the environment and to reduce greenhouse gas emissions.

According to Snyder et al. [7] nanofiltration or reverse osmosis is required to significantly reduce PPCP/EDCs levels in the wastewater. Nanofiltration and reverse osmosis require high pressure levels [8], leading to high energy consumption. On the other hand, Aldulgader et al. [9] reviewed hybrid processes for water resources, desalination and treatment of organic pollutants. They found that the hybrid processes have the potential to decrease the amount of discharge, as well as reduce the energy usage and costs. In a typical hybrid process, ion exchange resins are placed in vessels as steady packed beds, but Kabay et al. [10] introduced an exception. In their process, boron selective resins are mixed with feed water to sorb boron. After the sorption, saturated resins are separated from water with a membrane, and the permeate fulfills boron concentration requirements. Separated resins are regenerated and recycled back to the sorption phase. Aldulgader et al. [9] concluded that hybrid ion exchange-membrane processes have a place in solving the demands of wastewater treatment. In addition, a combination of ion exchange resin beads with membranes is one method to reduce PPCP/EDC levels in the wastewater ([11] and [12]).

Experimental research is a useful but labor intensive and expensive way to study the fluid-solid flow phenomenon in wastewater applications. However, the numerical methods offer a feasible tool for evaluating the flow phenomena before or in conjunction with experiments ([13] and [14]). Low costs, adaptability and possibility to obtain detailed information are the main reasons why computational fluid dynamics (CFD) are used to study wastewater applications, e.g. [15] and [16].

There are two main approaches in the modeling of the particulate phase in a dense fluid-particle system: the continuum approach, e.g. two fluid model

2

(TFM), or the discrete approach. Both of these methods base on so-called four-way coupling, which takes account fluid's effect on the particles, the particles' effect back to the fluid phase, the void fraction, and particle-particle interactions. The continuum approach assumes that the particles form an artificial continuum. The continuum approach loses the information of single particles and the closures that stem out from the kinetic theory of granular flow ([17] and [18]), are required to close the system of equations, e.g. momentum equation. A discrete approach, such as the discrete particle model (DPM), can overcome the limitations of TFM as particles are tracked in a Lagrangian frame and particle-particle interactions can be described with a simple spring-dashpot model. On the other hand, the DPM is computationally expensive compared to TFM or merely a one-way coupled discrete approach. Computational fluid dynamics-discrete element method (CFD-DEM), also referred to as a combined continuum and discrete model (CCDM) ([19] and [17]), is commonly used to obtain detailed information of the flow fields and the particle-particle interactions in gas-solid fluidized beds and pneumatic conveying ([20]). Liquid fluidized beds have been also studied with good agreement ([21], [22], [23], [24] and [25]). In the resent years, CFD-DEM has also been used to study particle batch settling ([26] and [27]), sediment transport ([28], [29], [30] and [31]), solid-liquid mixing ([32]) and slurry transport in pipes ([33], [34] and [35]). However, in the wastewater applications, due to the large size of the wastewater processing equipment and the low solid loading, the effect of the disperse phase on the carrier phase is neglected and one-way coupling is applied ([15] and [14]) to reduce the demand of computational resources.

The hybrid processes offer more compact and more energy efficient alternatives to wastewater treatment and reduction of PPCP/EDC levels ([9]). However, their development is still in its infancy and suitable validated computational tools are needed for the design and analysis. In the combined ion-exchange-membrane filtration, a layer of resin beads, called a bed, rests on top of a membrane and removes the contaminants before water permeates through the membrane film. The saturated ion-exchange resin beads can be removed

3

from the membrane, for example with backward or forward flushing (i.e. changing membrane flux direction or preventing membrane flux), and the be replaced with the slurry of the ion-exchange resin beads and water. In addition, to achieve a uniform pressure drop, the bed height and packing must be uniform. These requirements mean that to realize a working combined cycle, the hydrodynamics of the fluid-particle system and the effects of different parameters on its performance should be understood in detail.

Previously published studies show the CFD-DEM approach is mature and accurate method to model solid-liquid flows, therefore in this paper CFD-DEM method is applied to a new research area, wherein it has significant potential to enable reduction of energy usage and an increase in the wastewater quality. The novelty of the manuscript is twofold. Firstly, this study extends the utilization of CFD-DEM in the hydrodynamics of a combined ion exchange-membrane filtration, where it has not been used previously. Secondly, details on the bed formation and packing with insights on the parameters affecting these phenomena are presented. Finally, suggestions for improved hydrodynamic design of a combined ion exchange-membrane filtration are presented. The fouling of the membrane, as studied by Lohaus et al. [36] and ion exchange are not studied in this work.

Firstly, the applied CFD-DEM method is presented and method's capability to model solid volume fractions in heterogeneous slurry pipe flow is shown. Secondly, the investigated domain is introduced. Thirdly, the mesh independency study is presented and discussed. Then, the particle settling and bed formation is studied by changing the flow inlet velocity, the permeate flux, and the position of the particle insertion. Fourthly, the removal of the bed is investigated by back flushing. Finally, the results are summarized and the conclusions presented.

Nomenclature

Greek alphabet

α volume fraction   [-]

$\boldsymbol{\omega}$	angular velocity	[rad/s]
ϵ	turbulence dissipation rate	$[m^2/s^3]$
κ	turbulence kinetic energy	$[m^2/s^2]$
δ	overlap at the contact point	[m]
μ	dynamic viscosity	[Pas]
μ_C	Coulomb friction coefficient	[-]
ν	Poisson ration	[-]
ϕ	packing fraction	[-]
ρ	density	$[\text{kg}/m^3]$
τ	stress tensor	[Pa]

Latin alphabet

$\mathbf{F}$	force	[N]
$\mathbf{g}$	gravity	$[\text{m/s}^2]$
$\mathbf{I}$	rotational inertia	$[\text{kgm}^2]$
$\mathbf{R}$	momentum exchange term	$[\text{N/m}^3]$
$\mathbf{u}$	velocity	[m/s]
$\mathbf{x}$	coordinate	[m]
C	concentration	[-]
c	damping coefficient	[kg/s]
D	diameter of pipe	[m]
d_{50}	the midpoint of particle size distribution	[mm]
e	coefficient of restitution	[-]

5

120	F_L	parameter in the Durand equation	[-]
	k	spring stiffness	[N/m]
	K_f	momentum exchange coefficient	[kg/(m³s)]
	m	mass	[kg]
	r	radius	[m]
125	R_μ	rolling friction parameter	[-]
	T	torque	[Nm]
	t	time	[s]
	V	volume	[m³]
	Z	overall solid loading	[-]

130 Subscripts

	ν	viscous
	ave	average
	c	contact
	d	drag
135	f	fluid
	i	impact
	n	normal
	nor	normalized
	o	overall
140	p	particle
	pr	pressure

6

r	rolling	
re	relaxation	
rel	relative	
s	solid	
si	simulation	
su	superficial	
t	tangential	
tot	total	
ad	added mass	
mix	mixture	

2. Numerical methods

In this work, the translational and rotational motion of the solid phase are solved explicitly by the DEM package LIGGGHTS [37]. A particle trajectory is calculated based on the force and torque balance:

$$m_p\ddot{\mathbf{x}} = \mathbf{F}_n + \mathbf{F}_t + \mathbf{F}_d + \mathbf{F}_{pr} + \mathbf{F}_\nu + \mathbf{F}_g + \mathbf{F}_b \tag{1}$$

and

$$I_p\dot{\omega}_p = \mathbf{r}_{p,c} \times \mathbf{F}_t + \mathbf{T}_r \tag{2}$$

where m, $\mathbf{x}$ and $\mathbf{r}$ are mass, position and radius. $\mathbf{F}_n$ and $\mathbf{F}_t$ are the normal and tangential force due to particle-particle or particle-wall contact. $\mathbf{F}_d$ is the drag force that arises from the velocity difference of the fluid phase and particles. Particles are also affected by viscous force $\mathbf{F}_\nu$, pressure force $\mathbf{F}_{pr}$, buoyancy force $\mathbf{F}_b$ and gravity $\mathbf{F}_g$. $\mathbf{T}_r$ represents torque due to rolling friction.

Spring-dashpot model by Cundall and Strack [38] is used to define the particle contact forces. The spring represents elastic deformation while the viscous

7

dissipation is represented by the dashpot. The spring tension is calculated based on the overlap $\boldsymbol{\delta}$ of the two colliding particles. The normal force $\mathbf{F}_n$ and the magnitude of tangential force $\mathbf{F}_t$ are calculated as:

$$\mathbf{F}_n = -k_n\boldsymbol{\delta}_n + c_n\Delta\mathbf{u}_{p,n} \tag{3}$$

and

$$\mathbf{F}_t = \min\left(\left|k_t\int_{t_{c,0}}^{t}\Delta\boldsymbol{u}_{p,t}dt + c_t\Delta\boldsymbol{u}_{p,t}\right|, \mu_C\boldsymbol{F_n}\right) \tag{4}$$

where $\Delta\mathbf{u}_{p,n}$ and $\Delta\mathbf{u}_{p,t}$ are the relative normal and tangential velocities at contact, and $t_{c,0}$ is the start time of the contact. c_n and c_t are the normal and tangential damping coefficients. Coulomb friction coefficient μ_C is the limiting factor for maximum tangential force. The stiffness components and damping coefficients are calculated with simplified Hertz-Mindlin contact model ([39] and [40]).

Cohesive forces may have a effect to inter-particle forces in a certain application, for example with Geldart group C particles or in the membrane fouling study of Lohaust et al [36]. In this study, the size range of particles indicates that cohesive forces are neglectable and are therefore neglected.

Rolling friction is a natural torque that occurs in every rotating motion, which is one way to take into account non-sphericity of the particles. Ai et al. [41] categorized rolling resistance models into three classes: directional constant torque models, viscous models and elastic-plastic spring-dashpot models. In this study, one of the most common models, the directional constant torque model is used. This model uses a rolling friction parameter R_μ.

$$\mathbf{T}_r = R_\mu k_n\boldsymbol{\delta}\frac{\boldsymbol{\omega}_{rel}}{|\boldsymbol{\omega}_{rel}|}r_p \tag{5}$$

where the relative angular velocity $\boldsymbol{\omega}_{rel}$ is defined with angular velocity $\boldsymbol{\omega}$ and radius r:

$$\boldsymbol{\omega}_{rel} = \frac{r_i\boldsymbol{\omega}_i + r_j\boldsymbol{\omega}_j}{r_i + r_j} \tag{6}$$

The fluid phase is modeled with a non-resolved approach. This means that the particles are not resolved in the solution of the fluid phase, but their momentum

8

and mass are conserved. The volume-averaged Navier-Stokes equations (VANS) for the fluid phase is derived by Anderson and Jackson [42] and revised by Zhou et al. [43]. By following Zhou et al.'s [43] notation, the format set II of the VANS is used in this study:

$$\frac{\partial \alpha_f}{\partial t} + \nabla \cdot \left(\alpha_f \boldsymbol{u}_f\right) = 0 \tag{7}$$

$$\frac{\partial(\alpha_f \rho_f \boldsymbol{u}_f)}{\partial t} + \nabla \cdot \left(\alpha_f \rho_f \boldsymbol{u}_f \boldsymbol{u}_f\right) = -\alpha_f \nabla p + \boldsymbol{R}_f + \nabla \cdot \left(\alpha_f \boldsymbol{\tau}_f\right) \tag{8}$$

α_f and $\boldsymbol{u}_f$ are the volume fraction and the velocity, p is the pressure, ρ_f is the density and $\boldsymbol{\tau}_f$ is the viscous stress tensor of the fluid. $\boldsymbol{R}_f$ is momentum exchange term that accounts for forces between the fluid and particulate phase. The set II assumes that the pressure and viscous forces of the fluid are shared between the phases. This means that the particles are affected by pressure gradients and viscous shear forces, which are the independent of the drag force. These VANS are applied in CFD-DEM software by Goniva et al. [44] and the software is used in this study.

Though the solid stress tensors do not require a closure in the DEM method, an empirical or semi-empirical drag force has to be applied to the particles. In this study, the drag relation based on Koch and Hill's [45] Lattice Boltzmann simulations is applied:

$$\boldsymbol{F_d} = \frac{V_p \beta_f}{\alpha_s}(\boldsymbol{u}_f - \boldsymbol{u}_p) \tag{9}$$

$$\beta_f = \frac{18\mu(1 - \alpha_f)\alpha_f^2}{d_p^2}(F_0(\alpha_s) + 1/2 F_3(\alpha_s)Re_p) \tag{10}$$

$$Re_p = \frac{\alpha_f |\boldsymbol{u_f} - \boldsymbol{u_p}| d_p}{\nu} \tag{11}$$

$$
\begin{aligned}
F_0(\alpha_s) &= \frac{1 + 3\sqrt{\alpha_s/2} + (135/64)\alpha_s \ln(\alpha_s) + 16.14\alpha_s}{1 + 0.681\alpha_s - 5.48\alpha_s^2 + 8.16\alpha_s^3}, \alpha_s < 0.4 \\
F_0(\alpha_s) &= \frac{10\alpha_s}{(1 - \alpha_s)^3}, \alpha_s > 0.4
\end{aligned}
\tag{12}
$$

$$F_3 = 0.0673 + 0.212\alpha_s + \frac{0.0232}{(1 - \alpha_s)^5} \tag{13}$$

Pressure forces $\mathbf{F}_{pr}$ and viscous forces $\mathbf{F}_\nu$ can be expressed as (Crowe et al. [46]):

$$\mathbf{F}_{pr} = -V_p \nabla p \tag{14}$$

and

$$\mathbf{F}_\nu = -\nabla \cdot \tau_f V_p \tag{15}$$

where V_p is particle volume, p is pressure and τ is viscous stress tensor.

Gravity and buoyancy forces are formulated

$$\mathbf{F}_g + \mathbf{F}_b = (\rho_p - \rho_f)\boldsymbol{g}V_p \tag{16}$$

The relative velocity between the particles and fluid induces the drag force, which has a major impact on many solid-fluid flows, but other forces, e.g. virtual and Basset force, may have an impact on specific flows.

Added mass force adds inertia when relative acceleration occurs between particle and fluid. If the density of particles is decades larger than the density of fluid such as in gas-solid fluidization, the added mass force can be neglected ([47]). However, it is shown by Zhang et al. [48] that the added mass force has a strong effect to particle trajectories when the continuous phase is liquid. The added mass force was adopted in the liquid fluidization study by Potic et al. [22]. Similarly, the added mass force is also used by Sun and Xiao [30], and Uzi and Levy [35] in sediment and slurry transport studies. On the other hand, Di Renzo and Di Maio [23], Arolla and Desjardins [33], Capecelatro and Desjardis [34], and Blais et al. [49] have neglected the added mass force. The most common reason for neglecting the added mass force is the lack of expression for non-dilute particle flow regime, as Arolla and Desjardins [33] noted. The ratio between the drag force and the added mass force is estimated with a bead collision on a bead bed, which is a typical event in this study. In this collision,

10

the bead looses all of its kinetic energy and stays on the bed. The nominal fluid velocity of this study is used for the collision velocity and the timescale is estimated by contact duration. The contact duration is calculated by following the note of Legendre et al. [50]. The force ratio F_{ad}/F_d is $<< 1$, which indicates that the added mass force can be neglected. In addition, a simulation with the added mass force is performed and the averages of the drag force and added mass force are compared. The comparison indicates that the added mass force are two decades smaller than the drag force. Consequently, the added mass force is not taken into account in this work.

Formation of the viscous boundary layer on a particle surface generates the Basset or history force. As the Basset force being a result of time integration, it is computationally demanding ([51]). This force may be significant in the fluid field with strong oscillation, and its formations are derived for a single particle [46]. The force analysis is done to estimate the significance of the Basset force. A bead is accelerated from stationary to the nominal velocity of this study by using the particle relaxation time $\tau_{re,p}$. The drag force is several decades larger than the estimated Basset force, which indicates that the Basset force is not a major force. For this reason, the Basset force is neglected in this study.

The Saffman lift and Magnus effect are induced by velocity difference around a particle, the Saffman lift by the shear of fluid field, and the Magnus effect by the relative rotational velocity between a particle and the fluid. There are several expression for these forces in literature ([52], [53], and [54]). These models are derived for a single particle without the effect of volume fraction, and by neglecting the lift force, the deposition velocity is in better agreement with measurements ([55]). For these reasons, the lift forces are not included in this work. However, some of the lift effects are accounted by the pressure and viscous forces ([34]). By neglecting the Magnus effect, the rotational velocity of the particles is changed only during collision with other particles or a wall.

The momentum exchange term lays on the third Newtonian axiom and the same force acts on the solid and fluid phase but in the opposite directions. The

11

momentum exchange term $\boldsymbol{R}_f$ has two parts: explicit and implicit ([44]).

$$\boldsymbol{R_f} = K_f \boldsymbol{u}_f - K_f \langle \boldsymbol{u}_p \rangle \tag{17}$$

which uses the ensemble averaged particle velocity $\langle \boldsymbol{u}_p \rangle$ and the momentum exchange coefficient K_f

$$K_f = -\frac{|\sum \boldsymbol{F}_d|}{V_{cell} |\boldsymbol{u}_f - \langle \boldsymbol{u}_p \rangle|} \tag{18}$$

where V_{cell} is the volume of a fluid cell and the term $\sum \boldsymbol{F}_d$ sums all the particles' drag forces in the fluid cell. The viscous and pressure forces are not included into summation because these forces are taken into account directly in the VANS ([43]).

The simulation requires the CFD-DEM coupling routine and the algorithm to solve the pressure and velocity fields. The PISO method, which includes explicit velocity corrections, is used to solve the pressure and velocity fields of the fluid. Only a brief explanation about the coupling between CFD and DEM is presented here. The DEM solver calculates particle data, which is then transferred to CFD solver, where the forces and momentum of the fluid are calculated and new fluid fields are solved, after which the fluid-particle forces are sent to the DEM solver. Blais and Bertrand [49] have verified that the CFD solver produce divergence free solution. More details about the CFD-DEM coupling routine and the fluid solver can be found in ref. [37]. $\kappa - \epsilon$ turbulence model by Launder and Spalding [56] is used to model the fluid phase turbulence. This simple turbulence model is selected because the effect of turbulence in four-way coupling regime needs more clarification ([57, 58]).

The above-mentioned coupling routine includes steps which require the cell void fraction to have been defined before proceeding further. In other words, the Lagrangian property, a particle volume, has to be mapped to the Eulerian grid. In the simple mapping method, if the particle center is inside a cell, the whole volume of the particle is assumed to be inside the cell ([59]). This approach has two weaknesses. First, when a particle is close to a cell boundary, a major part of the particles volume can be appointed to the wrong cell. The

12

other weakness involves the violation of the non-resolved approach, i.e., when the particle size is close to the cell size, incorrect void fractions can occur, which have a negative effect to the model outputs and stability. To avoid the incorrect void fractions, several approaches have been applied. Peng et al. [21] used a particle meshing method (PMM) in which the particle is meshed to the small parts before each sub-part is mapped to cells according to the location of their centroids. In the offset method, used by Alobaid et al. [60] with a momentum and void fraction grid, the void fraction is defined with the Eulerian cell displacements and averaged across the calculated void fractions. In this study, a divided method, which has similarities with the PMM, is used to define the void fraction. In the divided method, a series of points that represent partial volumes are distributed in a particle and each point is mapped to the Eulerian grid ([37]).

3. Validation

The present method's capability model a horizontal pipe flow with solid material is tested against measurements by Gillies and Shook [61]. A pipe with inner diameter 0.0532 m is modeled with sand and water. The particle size distribution is presented by a single particle diameter to reduce computational demand. The measurements were performed on a closed loop device, but to decrease computational costs the, loop is replaced by a pipe with cyclic boundary conditions. The length of the simulated pipe was taken as 10 times of the inner diameter. Material properties are adopted from the study of Uzi and levy [35] and presented in Table 1. There are few exception from the material properties compared to Uzi and levy's [35] study. The Young modulus is decreased to increase the time step size, which is common way to decrease simulation time ([59]). The friction coefficient between particles is increased by following Wensrich and Katterfeld's [62] study and assuming an angle of repose of ~ 30 deg for sands.

13

Table 1: The geometry and material properties of pipe flow simulation

Property	Value	Unit
Geometry		
Pipe diameter	0.0532	m
Pipe length	0.532	m
DEM		
d_p	2.4	mm
ρ_p	2650	$\mathrm{kg/m^3}$
Y_p	4×10^9	Pa
Y_w	20×10^9	Pa
ν_p	0.17	-
ν_w	0.3	-
e_{p-p}	0.95	-
e_{p-w}	0.737	-
μ_{p-p}	0.3	-
μ_{p-w}	0.2	-
$R_{u,p-p}$	0.25	-
$R_{u,p-w}$	0.3	-
Fluid		
ρ_f	998	$\mathrm{kg/m^3}$
μ	1.0×10^{-3}	$\mathrm{m^2/s}$
Mixture		
u_{mix}	1.8 and 3.1	m/s
$\alpha_{s,tot}$	0.15	-

The particles are randomly initialized to the flow field that is driven by the pressure gradient between the ends of the pipe. Wall boundary condition is non-slip for the fluid phase. A particle-wall contact in DEM calculation is modeled similar way to a particle-particle contact, but the walls have infinite mass and radius in the contact calculation [63]. For the turbulent quantities of the fluid,

14

the wall functions by Kalitzin et al.[64] are applied. The mean fluid and solid velocities and the overlap are monitored during simulation to prevent excessive overlapping ($> 0.01d_p$) between particles and ensure the stable mean values. Over 100 mixture residue times, defined as L_{pipe}/u_{mix}, are used to form the mean values.

The simulated mean solid volume fractions and the measured results by Gillies and Shook [61] are presented in Figure 1 with mixture velocities 1.8 m/s and 3.1 m/s. In the same figure, Uzi and Levy's [35] CFD-DEM simulation results are also presented. In the measurements, on the bottom of pipe there is a dense region of solids, which decays along the height of pipe. The decay rate changes over pipe height, and the mean solid volume fractions form tilted S-shape. With the higher mixture velocity, the mean solid volume fraction is more uniform and the higher amount of particles are suspended in the upper part of the pipe. This is typical for heterogeneous suspended pipe flow. The present simulations can produce the trends of solid volume fraction profiles with both mixture velocities similar as Uzi and Levy's [35] CFD-DEM study. However, there is some disagreement with the measured results at the bottom and the upper parts of the pipe. The present simulations underestimate the mean solid volume fraction at the upper half of the pipe and overestimates at the bottom wall, especially with the mixture velocity 1.8 m/s. The results of Uzi and Levy's [35] CFD-DEM study are more align with the empirical results at mixture velocity 1.8 m/s. By following the force analyses of Uzi and Levy [35], the major part of difference in the results can be explained with different drag model and lower particle-particle friction fraction. As a result, the present method is capable of simulating and producing representative profiles of the solid volume fraction in solid-liquid flows, thus the present method can be utilized in the hydrodynamic design of the combined ion exchange-membrane filtration.
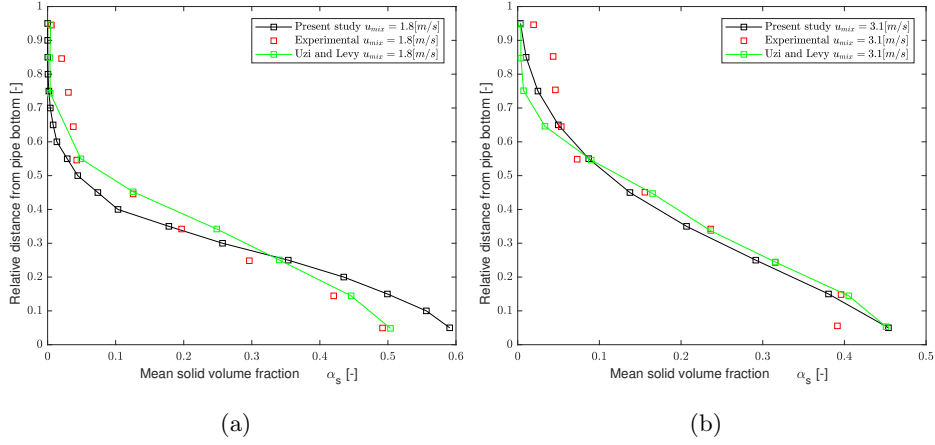
Figure 1: Simulated mean solid volume fractions with mixture velocities a) 1.8 m/s b) 3.1 m/s are compared to the measurements of Gillies and Shook [61].

4. Computational domain, material properties, and studied cases

A pseudo-2D calculation domain is used. The flow is modeled in 2D and the resin beads are calculated with the 3D slice. The 3D slice is used in a similar way as in the study by Ketterhagen et al. [65] to reduce the computational costs and include three dimensional effects. The depth of the 3D slice is $5d_p$. The computational domain is shown in Figure 2. The fluid flow with the resin beads is introduced in the left channel. A membrane that subtracts a part of the fluid is located between the backward- and forward-facing steps. The facing steps with the membrane form a region(red lines outline this volume in Figure 2) where some of the beads should settle on the membrane. This region is called a settling area. After the settling area, the rest of fluid and resin beads exit the domain on the right. A list of dimensions of the model domain is shown in Table 2. Solid phase boundary condition is same for the wall as in the validation simulation, periodic boundary condition is applied in the slice depth direction. The boundary conditions of the fluid solver side are presented in Table 3.

The resin bead's young modulus is estimated from the study by Tiihonen et al. [66]. The friction coefficient μ_c is 0.5 for bead-bead and bead-wall contact,
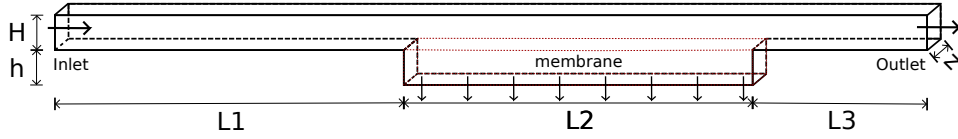
16

Figure 2: Outlay of computational domain. The black line outlines computational domain and the red line points out the volume of the interested, which is called as settling area.

base on polystyrene's coefficient of friction. The valuation of the coefficient of
340 restitution is more complicated in solid-liquid flow. Davis et al. [67] proposed a
dependency between the Stokes number, defined as $St_i = (\rho_p/\rho_f)Re_p/9$, and the
coefficient of restitution. Gondret et al. [47] confirmed in experiments that the
coefficient of restitution is strongly depend on Stokes numbers. Similar behavior
was also found by Kidanemarium and Uhlmann [29] with direct numerical sim-
345 ulation. Legendre et al. [50] proposed a model between the Stokes number and
the coefficient of restitution. Recently Biegert et al. [68] published a collision
model with a lubrication force that can model the squeezing of the liquid film
between particles or a wall. Despite of the lubrication force, the higher order
time integration and time sub-stepping was implemented by Biegert et al. [68]
350 to achieve good agreement with the experiments of Gondret et al. [47]. In addi-
tion, the lubrication force increases significantly computational demand ([30]).
Therefore, the reduced coefficient of restitution is used to model the lubrication
force, as done by Kidenemariam and Uhlmann [69] and Deshpande et al. [70]
in their studies. Same approach is applied in this study and the coefficient of
355 restitution, which is input parameter for DEM, is reduced and set to 0.3.

17

Table 2: Geometry and material properties

Property	Value	Unit
Geometry		
H	0.01	m
h	0.01	m
L1	0.1	m
L2	0.1	m
L3	0.05	m
z	0.001	m
DEM		
d_p	200	μm
ρ_p	1200	kg/m^3
Y_p	6.7×10^6	Pa
ν_p	0.34	-
$e_{p-p,p-w}$	0.3	-
$\mu_{p-p,p-w}$	0.5	-
$R_{u,p-p,p-w}$	0.0175	-
Fluid		
ρ_f	998	kg/m^3
μ	1.0×10^{-3}	m^2/s

Table 3: The boundary conditions for the liquid phase

	inlet	outlet	wall	membrane
α_f	fixedValue	zeroGradient	zeroGradient	zeroGradient
K_f	zeroGradient	zeroGradient	zeroGradient	zeroGradient
p	zeroGradient	fixedValue	zeroGradient	zeroGradient
$\boldsymbol{u}_f$	fixedValue	zeroGradient	non-slip	fixedValue
$\boldsymbol{u}_s$	zeroGradient	zeroGradient	zeroGradient	zeroGradient
ρ_f	zeroGradient	zeroGradient	zeroGradient	zeroGradient
k	fixedValue	zeroGradient	wallFunction	wallFunction
ϵ	fixedValue	zeroGradient	wallFunction	wallFunction

The effects of different variables and boundary values are investigated. In the first case, the boundary values for the superficial inlet velocity of the fluid are varied without allowing any flow through the membrane boundary. In the second case, a constant superficial inlet velocity is used and the fluid flow rate out of the system through the membrane is varied. In the third case, the height and the location of insertion of the beads is varied at the inlet channel. Finally, it the fourth case, flushing the resins off the membrane is studied with different fluid velocities through the membrane to the system. By default, the solid loading Z is fixed to 0.25 and the number of the inserted beads is set to 300,000, unless otherwise mentioned. The sum of beads' volume is 125% of the settling area's volume (red lines outline this volume in Figure 2). By assuming that the maximum packing fraction is 0.61 ([71]), the resin beads could fill the settling more than twice. A steady state fluid flow simulation without the beads is used to initialize the simulations. The membrane is modeled with a constant velocity boundary condition, similar to the study of de Jong et al. [72]. This simplification means that the pressure loss of the resin bead bed is negligible compared to transparent membrane pressure (TMP). The constants and variables are presented in Table 4 for each simulation.

19

Table 4: Different cases with fixed and varying parameters

Case 1

Changing variable:		
$V_{inlet,su}$, Range:	0.1–1	[m/s]
Fixed Variables:		
Z	0.25	[-]
Permeate flux	0	[m/s]

Case 2

Changing variable:		
Permeate flux, Range:	0–0.025	[m/s]
Fixed Variables:		
$V_{inlet,su}$	0.5	[m/s]
Z	0.25	[-]

Case 3

Changing variable:		
Position of bead insertion, Range:	Top, mid and bottom	
Fixed Variables:		
$V_{inlet,su}$	0.5	[m/s]
Permeate flux	0.015	[m/s]
Z	0.125	[-]

Case 4

Changing variable:		
Back flush; Permeate flux, Range:		
0, Stokes settling velocity (-0.0044) and -0.015		[m/s]
Fixed Variables:		
$V_{inlet,su}$	0.5	[m/s]
Z	0.25	[-]

Convection terms are spatially discretized with the quadratic upwind interpolation convection kinematics (QUICK) scheme. The time integration is

achieved using the backward scheme. The linear scheme is used for Laplacian terms.

Results are analyzed with normalized time t_{nor} and average packing fraction ϕ_{ave}. The normalized time is simulation time divided by the total simulation time $t_{nor} = t_{si}/t_{tot,si}$. Total simulation time $t_{tot,si}$ is the sum of the bead insertion time, which is the function of overall solid loading Z and the superficial velocity of water, and fluid residence time. The fluid residence time is the fluid's travel time from the inlet to the outlet with the inlet superficial velocity. The average packing fraction is the sum of resin beads' volume divided with the volume of the settling area $\Phi_{ave} = \frac{\sum V_{bead}}{V_{settling}}$

5. Mesh independency

A mesh independency study is more complicated to perform with multiphase simulations than single-phase simulations. The selected grid size affects the numerical stability through the exchange fields, i.e. void fraction and momentum transfer. In addition, drag closures are developed with an averaging process, whereby a certain amount of particles is assumed to fit into an averaged volume, e.g. Koch and Hill's [45] Lattice Boltzmann simulations. This combination can lead to a state where the mesh independency of the simulations results cannot be obtained. An example of this behavior can be seen from Figure 3 for case 2 with permeate flux 0.015 m/s. The mesh selected for further simulations contains 7,014 cells, using $3d_p$ spacing, which is same as in Ozel et al. [73] study. The selected mesh spacing is a tradeoff between discretization errors and void fraction errors, which arise from mapping between Lagrangian and Eulerian frames. The mesh is presented in Figure 4.

6. Results and discussion

6.1. Case 1: varying the superficial inlet velocity

The results of varying the superficial inlet velocity without any permeate flux are presented in Figure 5. The average packing fraction in the settling area
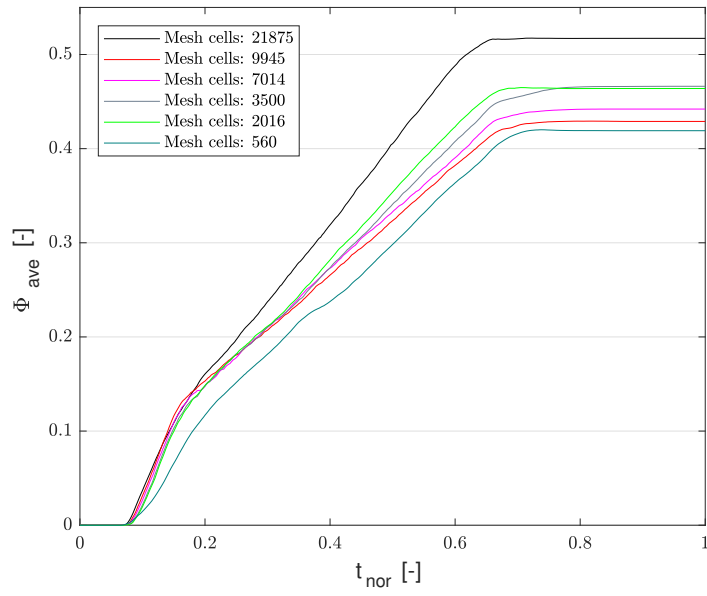
21

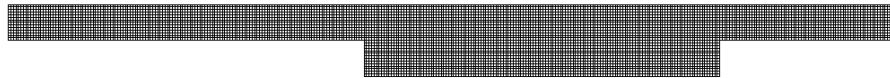Figure 3: The influence of mesh to average packing fraction with permeate flux 0.015 m/s.

Figure 4: The mesh used in the study.

is presented as a function of the normalized time. With the velocity 0.1 m/s, the average packing fraction increases steeply after the beads reach the settling area. The settling rate decreases at 0.2 in the normalized time, but the settling continues to t_{nor}= 0.8. After the bead insertion ends, the average packing fraction decreases. With the higher velocities 0.5 and 1.0 m/s, there are the same three phases as with the velocity 0.1 m/s, but the settling rates are lower and the average packing fractions stay under 0.15. Additionally, after the bead insertion the average packing fraction decreases more than with the velocity 0.1 m/s. The beads at the normalized time 0.5 are presented in Figure 6 with two velocities 1 m/s (a) and 0.1 m/s. With the higher velocity, there are no beads on the membrane surface and only a few beads are captured by a recirculation eddy, while with the lower velocity 0.1 m/s the corners are partially filled with beads and there is a thin bed on the membrane. The results are compared with the deposition velocity $v_D = 0.15 m/s$ and with the Froude number. Durand's [74] correlation for the deposition velocity is defined as:

$$v_D = F_L \sqrt{2gD(\frac{\rho_p}{\rho_f} - 1)} \tag{19}$$

where F_L is the parameter that takes into account the solid volume fraction and the diameter of the particles, and D is the characteristic diameter of the channel. Parameter F_L is calculated with Schiller and Herbich equation [75]:

$$F_L = 1.3 C_V^{0.125}(1 - e^{-6.9d_{50}}) \tag{20}$$

where C_V is solid concentration by volume and d_{50} is the midpoint of particle size distribution. The Froude number lies between 0.5 and 50, depending on the fluid velocity. The Froude and Durand's deposition velocity indicate that at the velocity 0.1 m/s, the gravitational force has a major effect on the beads and the beads are settling. On the other hand, the small Stokes number, defined as $St = \tau_{re,p}/\tau_{re,f}$ similarly to ref. [46], of < 1 explains the bead trajectories after the backward-facing step at the higher velocities. In the Figure 5, the decay of average packing fractions after the peak value can be explained by
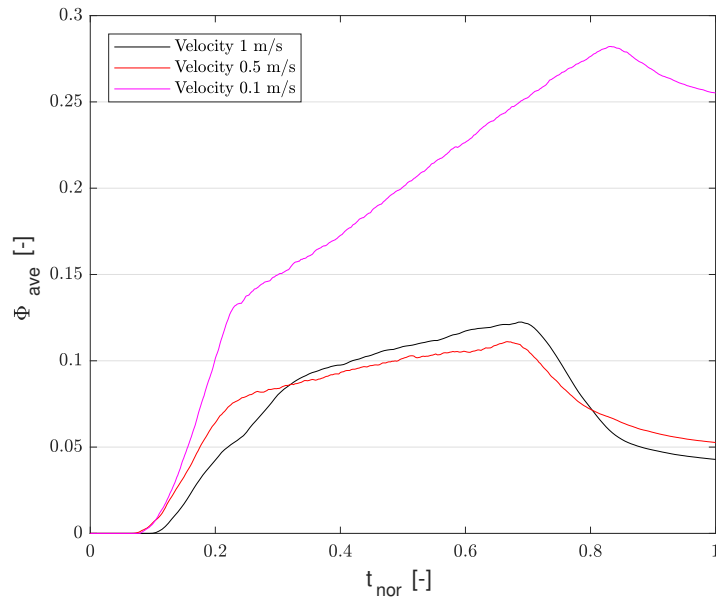
23

Figure 5: Overall packing fraction in the settling area with different inlet fluid velocities.

430 the recirculation eddy, which transports the beads to the main flow, and those beads are then transported out of the domain. Generally, the resin beads are held poorly in the settling area if the fluid velocity increases over the deposing velocity, and the other methods are required to form the resin bed.
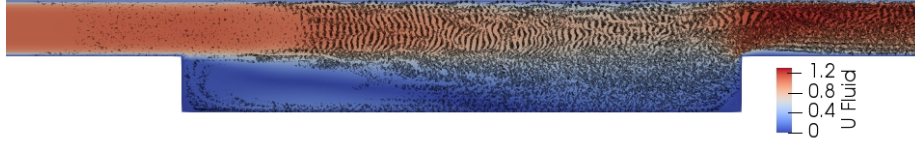
(a)
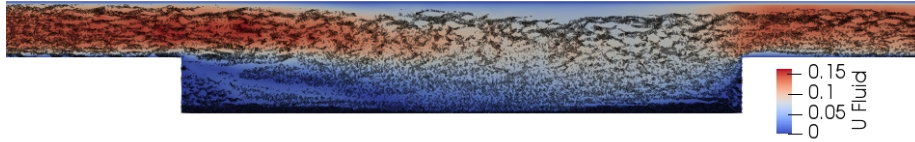
(b)

Figure 6: Resin beads are inserted with velocities 1 m/s (a) and 0.1 m/s (b). Snapshots are at the halfway point in the normalized time.

6.2. Case 2: fixed superficial inlet velocity with changing permeate flux

To achieve higher volumetric flow rates and to decrease the effect of the gravity on the bed formation, a higher superficial inlet velocity (0.5 m/s) than Duran's [76] deposing velocity correlation ($v_D = 0.15 m/s$) was selected for the permeate flux test. Figure 7 shows the average packing fraction in the settling area with varying permeate flux. The permeate flux varies from 0-0.025 m/s. In terms of the volumetric flow rate, the permeate flow rate is from 0% to 50% of the inlet flow rate. The permeate flux 0.015 m/s captures a major part of the inserted beads and a resin bead bed is formed. In other words, all the water does not need to pass through the membrane in order to form the bed in the settling area. Furthermore, with a permeate flux 0.01 m/s or less, there is a maximum in the average packing fraction. After the maximum, the non-settled beads are transported by the fluid from the settling area and the average packing fraction is stabilized. A similar phenomenon is not observed with the higher permeate

25

flux. Instead of a local maximum, steady average packing fractions are observed at the end of the bead insertion. With the highest (0.025 m/s) permeate flux, the settling area is fully packed with beads and the average packing fraction is in line with the maximum random packing fraction of spheres without the cohesive forces ([77]). The permeate flux has a major effect on the formation of the resin bead bed on the membrane. Figure 8 illustrates the shapes of the formed resin bead beds and supports the analysis of Figure 7. The height of the bed increases while the permeate flux increases, but the bed is not uniform. Filling starts next to the facing steps; see Figure 8 (a). The bed gets thicker from the backward-facing step to the forward-facing step, and the recirculation with the particle-particle friction forms a gap next to the backward-facing step; see Figure 8 (b). The recirculation brings beads next to the backward-facing step and the beads are in contact with other beads on the bed. In the contact, friction between beads stops the incoming bead and beads pile up. The slope of the pile, i.e., angle of repose, is the function of the fluid forces, gravity, and particle-particle forces. After the settling area is packed, the thickening bead bed decreases the flow area at the end of the inflow channel and the fluid velocity increases. The increasing fluid velocity prevents a total blocking of the flow channel and the bed stabilizes to its maximum thickness. In addition, the gap next to the backward-facing step is filled; see Figure 8 (c). As a result, the active resin bead bed can be achieved without dead-end packing, i.e., pushing all fluid through the membrane.
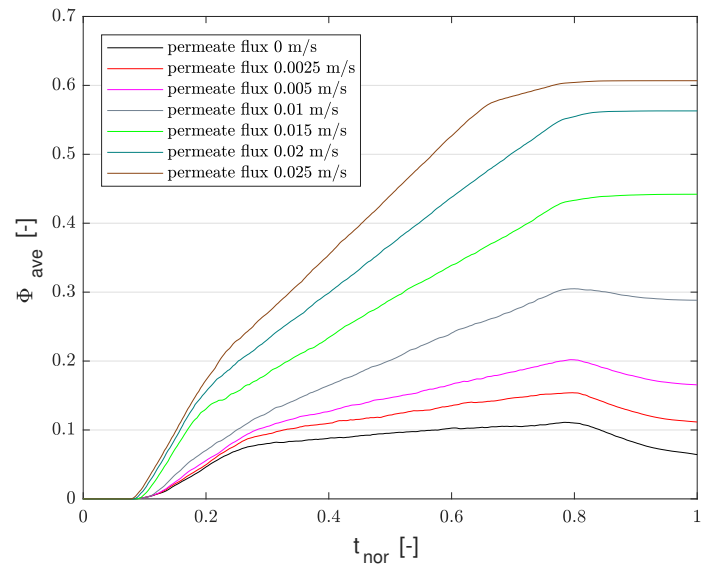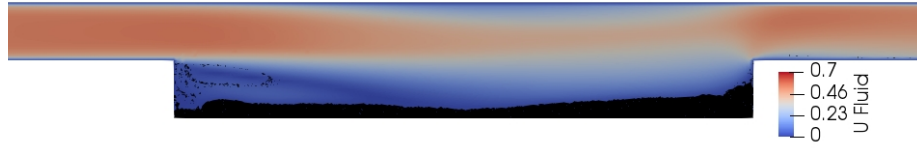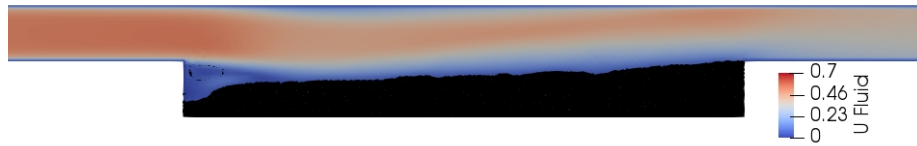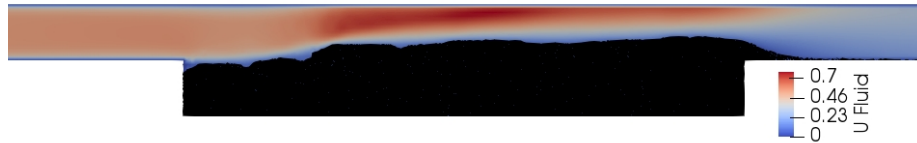
Figure 7: Average packing fraction in the settling area in time with varying permeate flux and constant inlet superficial flow velocity.

(a)

(b)

(c)

Figure 8: Constant inlet superficial velocity with permeate flux (a) 0.005 m/s (b) 0.015 m/s (c) 0.025 m/s. At the end of the simulation.

6.3. Case 3: the position of bead insertion in the inlet channel

The vertical position of the bead insertion is varied to study its effect to the bed formation. The bead insertion area is set to half of the inlet surface area, which means the overall solid loading Z needed to be decreased by 50 %. To point out the influence of the overall solid loading, a decreased overall loading $Z = 0.125$ with the whole inlet surface area is compared to a reference simulation, which is the case 2 with permeate flux 0.015 m/s. After comparing

the reference simulation and the decreased overall solid loading simulation, the decreased bead insertion area is varied in the vertical direction and compared to the decreased overall loading simulation. There are three positions for the half insertion area: the bottom, the middle and the top of the inlet channel.

Figure 9 presents the average packing fraction with the different bead insertion positions, the reference simulation and the decreased overall loading simulation with the respect to the normalized time. Comparing the settled beds at the end of the simulations, there is a negligible difference with the reference simulation and the decreased loading simulation. Based on this observation, the overall solid loading has little effect in the formation of the resin bead bed in this geometry in this case. However, the position of the bead insertion has a major effect to the formation of the bed (see Figures 9 and 10). If the beads are inserted from the bottom half of the inlet channel, there is a linear packing rate until Φ_{ave} is 0.5 and the rate decays to zero as Φ_{ave} reaches its maximum. With the insertion area in the middle of the inlet, a lower average packing fraction $\Phi_{ave}(0.2)$ is achieved when compared to other simulations or to the simulation where the beads are inserted at the bottom of the inlet channel. After the initial burst of beads to the settling area, the beads are settled on the membrane at a nearly linear rate until bead insertion ends. The insertion from the top of the inlet channel is an exception to the other cases. After the initial burst, the average packing fraction does not increase and nearly all the beads escape from the settling area after the end of the insertion. This can be explained by the Stokes number, as at low Stokes numbers (<1), the tracking error of the particles on the streamlines of the flow is small. The streamlines, which mainly start at the top of the inlet and end at the exit, carry the beads through the device without depositing the beads. In the other words, only those streamlines that end at the membrane transport beads on the membrane. In addition, all bead trajectories cannot be explained with low Stokes number because the collisions between the beads and walls affect to trajectories. To conclude, the position of the bead insertion has a major effect on the formation of the resin bead bed on the membrane, and it is recommended to insert beads near the bottom wall

29

of the inlet channel. Technically, inserting the resin beads into a certain area without mixing can be difficult.
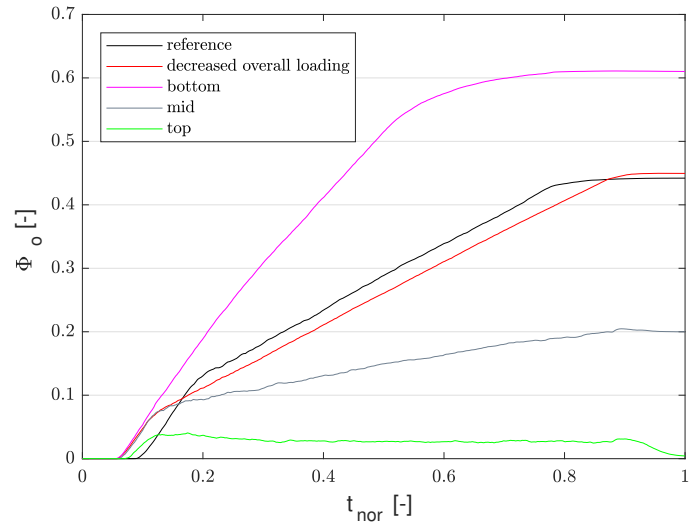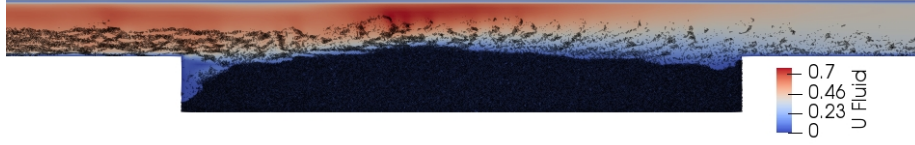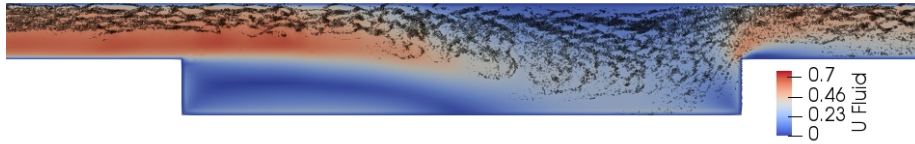

Figure 9: Influence of the bead insertion position in the inlet channel.

(a)

(b)

Figure 10: Comparison of the bottom (a) and top insertion positions at reduced time = 0.5. The major part of the inserted beads are settled on the bed with the bottom insertion but with the top insertion beads are carried away by the fluid.

6.4. Case 4: flushing

Back flushing is a common treatment method for restoring the membrane permeability. In this case, the aim of the back flushing is to remove the saturated or contaminated resin beads from the settling area. This can be done with and without back flushing. The bead bed is packed similarly to case 2 with a constant superficial inlet velocity of the fluid (0.5 m/s) and permeate flux 0.015 m/s. After the bed is formed, the direction of the fluid velocity at the membrane surface is reversed and three different velocities are used, namely 0 m/s (no back flushing), the Stokes settling velocity 0.0044 m/s, and the same velocity (0.015 m/s) as the in the packing phase. Figures 11 and 12 show the results of the packing and flushing phase. The packing phase is explained in the case 2. In the beginning of flushing, the rate of bead removal is high in Figure 11. After the initial burst, the rate of bead removal decays. With higher (0.015

31

m/s) back flushing, the initial burst removes more beads compared to other simulations and the decay rate is steeper. Practically, all beads are removed ₅₂₅ at 0.8 in the normalized time. The corners of the settling area are not cleared of the beads without back flushing (see Figure 12(a)) and some of the beads are captured in the recirculation eddy. With the Stokes settling velocity, there are no settled beads in the backward-facing step corner, recirculation holds the part of the beads, and few beads are remaining in the forward-facing step (see ₅₃₀ Figure 12b). Back flushing at 0.015 m/s removes the beads form the settling area, as can be seen from Figure 12c.

The flushing phase can be explained with two factors: the drag of flushing velocity and the forming recirculation eddy. In the simulation without the back flushing, the formation of the recirculation eddy starts after the uppermost ₅₃₅ beads are transported away from the bed by the fluid flow. The forming recirculation eddy lifts beads from the bed, which affects the flow fields of fluid. This phenomenon is visible in Figure 12a). With a back flushing at 0.015 m/s, the back flush pushes beads away from the settling area and the back flushing flux is high enough to prevent the formation of the recirculation eddy. With the Stokes ₅₄₀ settling velocity, the back flushing pushes beads from the corners, but it is not enough to prevent the formation of the recirculation eddy. The recirculation eddy captures some of the beads and loses them slowly to the main flow. To summarize, back flushing is needed to remove the beads from the corners of the settling area. The Stokes settling velocity as back flushing velocity is enough to ₅₄₅ remove the beads if there is enough time to empty the recirculation eddy. On the other hand, higher back flushing velocities than the Stokes settling velocity prevent the formation of the recirculation eddy and remove the bed faster.
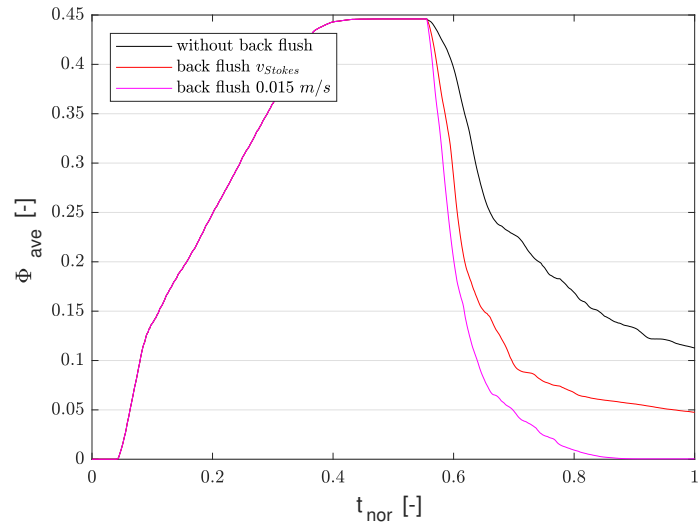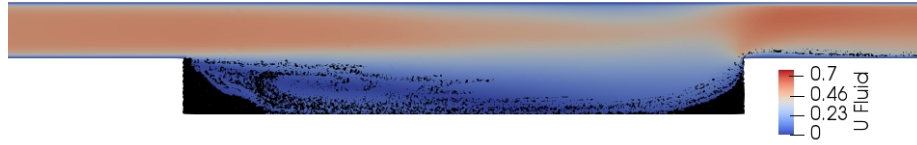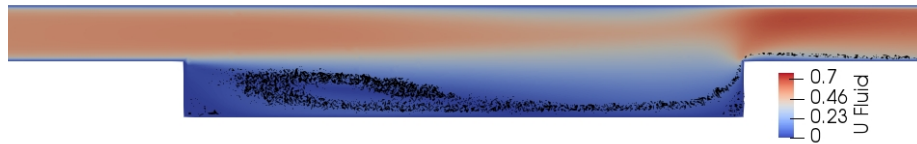
Figure 11: Removing beads from the settling area with and without back flushing

(a)

(b)

(c)

Figure 12: At the end of back flushing a) with zero velocity b) with Stokes settling velocity (0.0044 m/s) c) with velocity 0.015 m/s

7. Conclusion

This study demonstrates how the computational fluid dynamic-discrete ele-
ment method is applied to analyze and study the hydrodynamics of combined ion
exchange-membrane filtration, which is a new application area for this method.
The test scale model of this filtration method is selected for the demonstration.
The details on the bed formation and the parameters affecting it are analyzed

34

by varying the fluid velocity, membrane flux, position of bead insertion, and back flushing. Based on the analyzed parameters, the following suggestions for the hydrodynamic design can be presented:

- Inlet velocities under the Durand's depositing velocity have to be used to form the resin bead bed when there is no flow through the membrane.

- Higher inlet velocities can be used if a part of the fluid is flowing through the membrane.

- The position of the bead insertion has a large influence on the formation of the filtration bed. This is because particles with small Stokes number follow the streamlines of the fluid. Thus, for the bed formation, it is beneficially to insert the beads closer to the membrane.

- Back flushing has to used for the removal of the beads from the corners, and Stokes settling velocity is in the correct range for the back flushing velocity.

- Settling velocity plays a major role in the design of the combined ion exchange-membrane filtration system.

While detailed measurements of the flow fields are required to validate the simulations, the presented results are reasonable, especially when considering the Stokes settling velocity and Durand's depositing velocity. The presented computational approach is capable of capturing phenomena in the solid-liquid flow at a very detailed level, even granular phase's capability to form force-chains, i.e., form piles. The presented method seems highly applicable for studying the hydrodynamics of particle-water mixtures in wastewater applications that are aimed for the reduction of harmful emissions and improve water quality.

References

[1] Y. Sun, H. Huang, Y. Sun, C. Wang, X.-L. Shi, H.-Y. Hu, T. Kameya, K. Fujie, Ecological risk of estrogenic endocrine disrupting chemicals in sewage plant effluent and reclaimed water, Environmental Pollution 180 (2013) 339 – 344. `doi:10.1016/j.envpol.2013.05.006`.

[2] W. Ma, C. Nie, B. Chen, X. Cheng, X. Lun, F. Zeng, Adsorption and biodegradation of three selected endocrine disrupting chemicals in river-based artificial groundwater recharge with reclaimed municipal wastewater, Journal of Environmental Sciences 31 (2015) 154 – 163. `doi:10.1016/j.jes.2014.12.006`.

[3] Y. Yoon, P. Westerhoff, S. A. Snyder, M. Esparza, Hplc-fluorescence detection and adsorption of bisphenol a, 17-estradiol, and 17-ethynyl estradiol on powdered activated carbon, Water Research 37 (14) (2003) 3530 – 3537. `doi:10.1016/S0043-1354(03)00239-2`.

[4] A. Belfroid, A. V. der Horst, A. Vethaak, A. Schfer, G. Rijs, J. Wegener, W. Cofino, Analysis and occurrence of estrogenic hormones and their glucuronides in surface water and waste water in the netherlands, Science of The Total Environment 225 (12) (1999) 101 – 108. `doi:10.1016/S0048-9697(98)00336-2`.

[5] T. Ternes, M. Stumpf, J. Mueller, K. Haberer, R.-D. Wilken, M. Servos, Behavior and occurrence of estrogens in municipal sewage treatment plants i. investigations in germany, canada and brazil, Science of The Total Environment 225 (12) (1999) 81 – 90. `doi:10.1016/S0048-9697(98)00334-9`.

[6] H. M. Kuch, K. Ballschmiter, Determination of endocrine-disrupting phenolic compounds and estrogens in surface and drinking water by hrgc(nci)ms in the picogram per liter range, Environmental Science & Technology 35 (15) (2001) 32013206.

36

[7] S. A. Snyder, S. Adham, A. M. Redding, F. S. Cannon, J. DeCarolis, J. Oppenheimer, E. C. Wert, Y. Yoon, Role of membranes and activated carbon in the removal of endocrine disruptors and pharmaceuticals, Desalination 202 (13) (2007) 156 – 181, wastewater Reclamation and Reuse for Sustainability. doi:10.1016/j.desal.2005.12.052.

[8] Y. Yoon, P. Westerhoff, S. A. Snyder, E. C. Wert, J. Yoon, Removal of endocrine disrupting compounds and pharmaceuticals by nanofiltration and ultrafiltration membranes, Desalination 202 (13) (2007) 16 – 23, wastewater Reclamation and Reuse for Sustainability. doi:10.1016/j.desal.2005.12.033.

[9] H. A. Abdulgader, V. Kochkodan, N. Hilal, Hybrid ion exchange pressure driven membrane processes in water treatment: A review, Separation and Purification Technology 116 (2013) 253 – 264. doi:10.1016/j.seppur.2013.05.052.

[10] N. Kabay, dil Yilmaz, M. Bryjak, M. Yksel, Removal of boron from aqueous solutions by a hybrid ion exchangemembrane process, Desalination 198 (1) (2006) 158 – 165, the Second Membrane Science and Technology Conference of Visegrad Countries (PERMEA 2005). doi:10.1016/j.desal.2006.09.011.

[11] K. Laatikainen, M. Laatikainen, M. Bryjak, T. Sainio, H. Siren, Adsorption of bisphenol a from water-ethanol mixtures on pulverized activated carbon, Separation Science and Technology 49 (5) (2014) 763–772. doi:10.1080/01496395.2013.860462.

[12] J. Wolska, M. Bryjak, Removal of bisphenol a from aqueous solution by molecularly imprinted polymers, Separation Science and Technology 49 (11) (2014) 1643–1653. doi:10.1080/01496395.2014.906459.

[13] D. L. Huggins, R. H. Piedrahita, T. Rumsey, Use of computational fluid dynamics (cfd) for aquaculture raceway design to increase settling ef-

37

fectiveness, Aquacultural Engineering 33 (3) (2005) 167 – 180. `doi:`
`10.1016/j.aquaeng.2005.01.008`.

[14] M. Al-Sammarraee, A. Chan, S. Salim, U. Mahabaleswar, Large-eddy simulations of particle sedimentation in a longitudinal sedimentation basin of a water treatment plant. part i: Particle settling performance, Chemical Engineering Journal 152 (23) (2009) 307 – 314. `doi:10.1016/j.cej.2009.` `04.062`.

[15] R. Tarpagkou, A. Pantokratoras, {CFD} methodology for sedimentation tanks: The effect of secondary phase on fluid phase using {DPM} coupled calculations, Applied Mathematical Modelling 37 (5) (2013) 3478 – 3494. `doi:10.1016/j.apm.2012.08.011`.

[16] M. Dufresne, J. Vazquez, A. Terfous, A. Ghenaim, J.-B. Poulet, Experimental investigation and {CFD} modelling of flow, sedimentation, and solids separation in a combined sewer detention tank, Computers & Fluids 38 (5) (2009) 1042 – 1049, advances in Computational Fluid Dynamics 9th International Conference on Fluid Control, Measurements, and Visualization. `doi:10.1016/j.compfluid.2008.01.011`.

[17] N. Deen, M. V. S. Annaland, M. V. der Hoef, J. Kuipers, Review of discrete particle modeling of fluidized beds, Chemical Engineering Science 62 (12) (2007) 28 – 44, fluidized Bed Applications. `doi:10.1016/j.ces.2006.08.` `014`.

[18] R. A. Bell, Numerical modelling of multi-particle flows in bubbling gas-solid fluidised beds, Swinburne University of Technology, 2000.

[19] K. Chu, A. Yu, Numerical simulation of complex particlefluid flows, Powder Technology 179 (3) (2008) 104 – 114, {WCPT5} Papers presented at the 5th World Conference of Particle Technology (WCPT5), Orlando, Florida, April 2327 2006 5th World Conference of Particle Technology (WCPT5). `doi:10.1016/j.powtec.2007.06.017`.

[20] H. Zhu, Z. Zhou, R. Yang, A. Yu, Discrete particle simulation of particulate systems: A review of major applications and findings, Chemical Engineering Science 63 (23) (2008) 5728 – 5770. `doi:10.1016/j.ces.2008.08.006`.

[21] Z. Peng, S. V. Ghatage, E. Doroodchi, J. B. Joshi, G. M. Evans, B. Moghtaderi, Forces acting on a single introduced particle in a solidliquid fluidised bed, Chemical Engineering Science 116 (0) (2014) 49 – 70. `doi:10.1016/j.ces.2014.04.040`.

[22] B. Potic, S. Kersten, M. Ye, M. van der Hoef, J. Kuipers, W. van Swaaij, Fluidization with hot compressed water in micro-reactors, Chemical Engineering Science 60 (22) (2005) 5982 – 5990, 7th International Conference on Gas-Liquid and Gas-Liquid-Solid Reactor Engineering. `doi:10.1016/j.ces.2005.04.047`.

[23] A. D. Renzo, F. P. D. Maio, Homogeneous and bubbling fluidization regimes in demcfd simulations: Hydrodynamic stability of gas and liquid fluidized beds, Chemical Engineering Science 62 (1) (2007) 116 – 130, fluidized Bed Applications. `doi:10.1016/j.ces.2006.08.009`.

[24] M. van Sint Annaland, N. Deen, J. Kuipers, Numerical simulation of gasliquidsolid flows using a combined front tracking and discrete particle method, Chemical Engineering Science 60 (22) (2005) 6188 – 6198, 7th International Conference on Gas-Liquid and Gas-Liquid-Solid Reactor Engineering. `doi:10.1016/j.ces.2005.04.038`.

[25] J. Zhang, Y. Li, L.-S. Fan, Discrete phase simulation of gasliquidsolid fluidization systems: single bubble rising behavior, Powder Technology 113 (3) (2000) 310 – 326, neptis Symposium on Fluidization- Present and Future. `doi:10.1016/S0032-5910(00)00314-4`.

[26] R.-Q. Wang, A. W.-K. Law, E. E. Adams, Large-eddy simulation (les) of settling particle cloud dynamics, International Journal of Multiphase Flow 67 (0) (2014) 65 – 75. `doi:10.1016/j.ijmultiphaseflow.2014.08.004`.

[27] T. Zhao, G. T. Houlsby, S. Utili, Investigation of granular batch sedimentation via dem–cfd coupling, Granular Matter 16 (6) (2014) 921–932. `doi:10.1007/s10035-014-0534-0`.

[28] H. Elghannay, D. Tafti, Les-dem simulations of sediment transport, International Journal of Sediment Research 33 (2) (2018) 137 – 148. `doi:10.1016/j.ijsrc.2017.09.006`.

[29] A. G. Kidanemariam, M. Uhlmann, Interface-resolved direct numerical simulation of the erosion of a sediment bed sheared by laminar channel flow, International Journal of Multiphase Flow 67 (0) (2014) 174 – 188. `doi:10.1016/j.ijmultiphaseflow.2014.08.008`.

[30] R. Sun, H. Xiao, Sedifoam: A general-purpose, open-source cfddem solver for particle-laden flow with emphasis on sediment transport, Computers & Geosciences 89 (2016) 207 – 219. `doi:10.1016/j.cageo.2016.01.011`.

[31] M. Dallali, V. Armenio, Large eddy simulation of two-way coupling sediment transport, Advances in Water Resources 81 (2015) 33 – 44, fluvial Eco-Hydraulics And Morphodynamics. `doi:10.1016/j.advwatres.2014.12.004`.

[32] B. Blais, O. Bertrand, L. Fradette, F. Bertrand, Cfd-dem simulations of early turbulent solidliquid mixing: Prediction of suspension curve and just-suspended speed, Chemical Engineering Research and Design 123 (2017) 388 – 406. `doi:10.1016/j.cherd.2017.05.021`.

[33] S. K. Arolla, O. Desjardins, Transport modeling of sedimenting particles in a turbulent pipe flow using eulerlagrange large eddy simulation, International Journal of Multiphase Flow 75 (2015) 1 – 11. `doi:10.1016/j.ijmultiphaseflow.2015.04.010`.

[34] J. Capecelatro, O. Desjardins, Eulerianlagrangian modeling of turbulent liquidsolid slurries in horizontal pipes, International Journal of Multiphase Flow 55 (2013) 64 – 79. `doi:10.1016/j.ijmultiphaseflow.2013.04.006`.

40

[35] A. Uzi, A. Levy, Flow characteristics of coarse particles in horizontal hydraulic conveying, Powder Technology 326 (2018) 302 – 321. `doi:10.1016/j.powtec.2017.11.067`.

[36] J. Lohaus, Y. Perez, M. Wessling, What are the microscopic events of colloidal membrane fouling?, Journal of Membrane Science 553 (2018) 90 – 98. `doi:10.1016/j.memsci.2018.02.023`.

[37] C. Kloss, C. Goniva, A. Hager, S. Amberger, S. Pirker, Models, algorithms and validation for opensource dem and cfd-dem, Progress in Computational Fluid Dynamics 12 (2-3) (2012) 140–152. `doi:10.1504/PCFD.2012.047457`.

[38] P. Cundall, O. Strack, A discrete numerical model for granular assemblies, Gotechnique 29 (1) (1979) 47 – 65. `doi:10.1680/geot.1979.29.1.47`.

[39] Y. Tsuji, T. Tanaka, T. Ishida, Lagrangian numerical simulation of plug flow of cohesionless particles in a horizontal pipe, Powder Technology 71 (3) (1992) 239 – 250. `doi:https://doi.org/10.1016/0032-5910(92)88030-L`.

[40] A. D. Renzo, F. P. D. Maio, Comparison of contact-force models for the simulation of collisions in dem-based granular flow codes, Chemical Engineering Science 59 (3) (2004) 525 – 541. `doi:10.1016/j.ces.2003.09.037`.

[41] J. Ai, J.-F. Chen, J. M. Rotter, J. Y. Ooi, Assessment of rolling resistance models in discrete element simulations, Powder Technology 206 (3) (2011) 269 – 282. `doi:10.1016/j.powtec.2010.09.030`.

[42] T. Anderson, R. Jackson, A fluid mechanical description of fluidized beds: Equations of motion, Industrial and Engineering Chemistry Fundamentals 6 (4) (1967) 527–539.

[43] Z. Y. Zhou, S. B. Kuang, K. W. Chu, A. B. Yu, Discrete particle simulation of particlefluid flow: model formulations and their applicability, Journal of Fluid Mechanics 661 (2010) 482510. `doi:10.1017/S002211201000306X`.

41

[44] C. Goniva, C. Kloss, N. G. Deen, J. A. Kuipers, S. Pirker, Influence of rolling friction on single spout fluidized bed simulation, Particuology 10 (5) (2012) 582 – 591. `doi:10.1016/j.partic.2012.05.002`.

[45] D. Koch, R. Hill, Inertial effects in suspension and porous-media flows, Annual Review of Fluid Mechanics 33 (2001) 619–647.

[46] C. Crowe, J. Schwarzkopf, M. Sommerfeld, Y. Tsuji, Multiphase Flows with Droplets and Particles, Second Edition, Boca Raton: CRC Press, 2011.

[47] P. Gondret, M. Lance, L. Petit, Bouncing motion of spherical particles in fluids, Physics of Fluids 14 (2) (2002) 643–652. `doi:10.1063/1.1427920`.

[48] J. Zhang, L.-S. Fan, C. Zhu, R. Pfeffer, D. Qi, Dynamic behavior of collision of elastic spheres in viscous fluids, Powder Technology 106 (1) (1999) 98 – 109. `doi:10.1016/S0032-5910(99)00053-4`.

[49] B. Blais, F. Bertrand, On the use of the method of manufactured solutions for the verification of {CFD} codes for the volume-averaged navierstokes equations, Computers & Fluids 114 (0) (2015) 121 – 129. `doi:10.1016/j.compfluid.2015.03.002`.

[50] D. Legendre, R. Zenit, C. Daniel, P. Guiraud, A note on the modelling of the bouncing of spherical drops or solid spheres on a wall in viscous fluid, Chemical Engineering Science 61 (11) (2006) 3543 – 3549. `doi:10.1016/j.ces.2005.12.028`.

[51] H. A. Elghannay, D. K. Tafti, Development and validation of a reduced order history force model, International Journal of Multiphase Flow 85 (2016) 284 – 297. `doi:10.1016/j.ijmultiphaseflow.2016.06.019`.

[52] P. G. Saffman, The lift on a small sphere in a slow shear flow, Journal of Fluid Mechanics 22 (2) (1965) 385400. `doi:10.1017/S0022112065000824`.

[53] E. Loth, A. J. Dorgan, An equation of motion for particles of finite reynolds number and size, Environmental Fluid Mechanics 9 (2) (2009) 187–206. `doi:10.1007/s10652-009-9123-x`.

[54] D. Z. Zhang, A. Prosperetti, Averaged equations for inviscid disperse two-phase flow, Journal of Fluid Mechanics 267 (1994) 185219. `doi:10.1017/S0022112094001151`.

[55] Q. Wang, K. Squires, M. Chen, J. McLaughlin, On the role of the lift force in turbulence simulations of particle deposition, International Journal of Multiphase Flow 23 (4) (1997) 749 – 763. `doi:10.1016/S0301-9322(97)00014-1`.

[56] B. Launder, D. Spalding, The numerical computation of turbulent flows, Computer Methods in Applied Mechanics and Engineering 3 (2) (1974) 269 – 289. `doi:10.1016/0045-7825(74)90029-2`.

[57] S. Elghobashi, On predicting particle-laden turbulent flows, Applied Scientific Research 52 (4) (1994) 309–329. `doi:10.1007/BF00936835`.

[58] S. Elghobashi, An Updated Classification Map of Particle-Laden Turbulent Flows, Springer, Netherlands, 2006.

[59] Y. Tsuji, T. Kawaguchi, T. Tanaka, Discrete particle simulation of two-dimensional fluidized bed, Powder Technology 77 (1) (1993) 79–87. `doi:10.1016/0032-5910(93)85010-7`.

[60] F. Alobaid, J. Strhle, B. Epple, Extended cfd/dem model for the simulation of circulating fluidized bed, Advanced Powder Technology 24 (1) (2013) 403 – 415. `doi:10.1016/j.apt.2012.09.003`.

[61] R. G. Gillies, C. A. Shook, Concentration distributions of sand slurries in horizontal pipe flow, Particulate Science and Technology 12 (1) (1994) 45–69. `doi:10.1080/02726359408906641`.

[62] C. Wensrich, A. Katterfeld, Rolling friction as a technique for modelling particle shape in dem, Powder Technology 217 (2012) 409 – 417. `doi:10.1016/j.powtec.2011.10.057`.

[63] T. Pschel, T. Schwager, Computational Granular Dynamics, Springer Berlin Heidelberg, 2005. `doi:10.1007/3-540-27720-X`.

[64] G. Kalitzin, G. Medic, G. Iaccarino, P. Durbin, Near-wall behavior of rans turbulence models and implications for wall functions, Journal of Computational Physics 204 (1) (2005) 265 – 291. `doi:https://doi.org/10.1016/j.jcp.2004.10.018`.

[65] W. R. Ketterhagen, J. S. Curtis, C. R. Wassgren, B. C. Hancock, Modeling granular segregation in flow from quasi-three-dimensional, wedge-shaped hoppers, Powder Technology 179 (3) (2008) 126 – 143, {WCPT5} Papers presented at the 5th World Conference of Particle Technology (WCPT5), Orlando, Florida, April 2327 2006 5th World Conference of Particle Technology (WCPT5). `doi:10.1016/j.powtec.2007.06.023`.

[66] J. Tiihonen, I. Markkanen, M. Laatikainen, E. Paatero, Elasticity of ion-exchange resin beads in solvent mixtures, Journal of Applied Polymer Science 82 (5) (2001) 1256–1264. `doi:10.1002/app.1959`.

[67] R. H. Davis, J.-M. Serayssol, E. J. Hinch, The elastohydrodynamic collision of two spheres, Journal of Fluid Mechanics 163 (1986) 479497. `doi:10.1017/S0022112086002392`.

[68] E. Biegert, B. Vowinckel, E. Meiburg, A collision model for grain-resolving simulations of flows over dense, mobile, polydisperse granular sediment beds, Journal of Computational Physics 340 (2017) 105 – 127. `doi:10.1016/j.jcp.2017.03.035`.

[69] A. Kidanemariam, M. Uhlmann, Direct numerical simulation of pattern formation in subaqueous sediment, Journal of Fluid Mechanics 750 (2014) R2. `doi:10.1017/jfm.2014.284`.

[70] R. Deshpande, S. Antonyuk, O. Iliev, Study of the filter cake formed due to the sedimentation of monodispersed and bidispersed particles using discrete

element methodcomputational fluid dynamics simulations, AIChE Journal 0 (0). `doi:10.1002/aic.16529`.

[71] S. Torquato, T. M. Truskett, P. G. Debenedetti, Is random close packing of spheres well defined?, Phys. Rev. Lett. 84 (2000) 2064–2067. `doi:10.1103/PhysRevLett.84.2064`.

[72] J. de Jong, T. Dang, M. van Sint Annaland, J. Kuipers, Comparison of a discrete particle model and a two-fluid model to experiments of a fluidized bed with flat membranes, Powder Technology 230 (0) (2012) 93 – 105. `doi:10.1016/j.powtec.2012.06.059`.

[73] A. Ozel, J. Kolehmainen, S. Radl, S. Sundaresan, Fluid and particle coarsening of drag force for discrete-parcel approach, Chemical Engineering Science 155 (2016) 258 – 267. `doi:10.1016/j.ces.2016.08.014`.

[74] R. Durand, Basic relationships of the transportation of solids in pipes-experimental research, Proceedings of the International Association of Hydraulic Research (1953) 89–103.

[75] R. E. Schiller, P. E. Herbich, Sediment transport in pipes, In Handbook of Dredging, McGraw-Hill, 1991.

[76] R. C. Worster, D. F. Denny, Hydraulic transport of solid material in pipes, Proceedings of the Institution of Mechanical Engineers 169 (1) (1955) 563–586. `doi:10.1243/PIME\_PROC\_1955\_169\_064\_02`.

[77] K. J. Dong, R. Y. Yang, R. P. Zou, A. B. Yu, Settling of particles in liquids: Effects of material properties, AIChE Journal 58 (5) (2012) 1409–1421. `doi:10.1002/aic.12682`.